Phys Chem Minerals (2003) 30: 44 – 53
DOI 10.1007/s00269-002-0286-y

ORIGINAL PAPER

D. Vantelon · E. Montarges-Pelletier · L. J. Michot
V. Briois · M. Pelletier · F. Thomas

Iron distribution in the octahedral sheet of dioctahedral smectites. An Fe K-edge X-ray absorption spectroscopy study

Received: 21 January 2002 / Accepted: 23 October 2002

Abstract The distribution of iron atoms in the octahedral sheet of a series of dioctahedral smectites with varying unit-cell composition and iron content was investigated by Fe K-edge XAS spectroscopy. First-step analysis reveals that the patterns corresponding to backscattering by atoms located between 3 and 4 Å from the absorbing atom are very sensitive to the relative amount of light (Si, Al, Mg) and heavy (Fe) atoms. Detailed modelling of this domain then provides valuable information on the number of iron atoms surrounding octahedral iron. By comparing the number of iron neighbours deduced from EXAFS with that determined from unit-cell composition assuming a statistical distribution, three groups of montmorillonites can be distinguished: (1) clay samples from Wyoming display an ordered distribution of iron atoms; (2) clay samples from Georgia, Milos, China and Washington exhibit a close to random distribution of iron atoms; (3) clay samples from North Africa, Germany, Texas and Arizona display extensive iron clustering. These results complement previously obtained IR results and show that the combination of these two spectroscopic techniques could provide an additional crystal-chemistry-based framework for typological analysis of montmorillonite deposits.

D. Vantelon · E. Montarges-Pelletier (✉) · L. J. Michot
M. Pelletier · F. Thomas
Laboratoire Environnement et Minéralurgie,
UMR 7569 CNRS-INPL, Pôle de l'Eau,
15 av. du Charmois, 54501 Vandoeuvre-lès-Nancy Cedex, France
Tel.: +33-0383-596252
Fax: +33-0383-596255
e-mail: emont@ensg.inpl-nancy.fr

V. Briois
Laboratoire pour l'Utilisation du Rayonnement
Electromagnétique, CNRS UMR 130, BP 34, 91898 Orsay, France

Present address: D. Vantelon
Department of Soil Chemistry, ITO-ETHZ,
Grabenstrasse 3, 8952 Schlieren, Switzerland

Keywords Montmorillonite · EXAFS · Iron · Octahedral

Introduction

Montmorillonite, the most common smectite clay mineral, exhibits a wide variation in chemical composition as a result of compositional variability of the tetrahedral and mainly the octahedral sheet. Furthermore, even for similar compositions, the ordering of the distribution of cations can be very different, especially in the octahedral layer. Layer charge of such minerals is essentially located in the octahedral sheet. Thus, ordering in the octahedral layer clearly deserves particular attention, as it should play a role in controlling the colloidal properties of montmorillonites. However, determining the actual cation distribution in these minerals is a rather complex problem. It can be at least partially solved by using various spectroscopic tools. Among spectroscopic techniques, infrared (IR) spectroscopy has been shown to be one of the most effective methods for studying short-range ordering in the distribution of cations in phyllosilicates (Fripiat 1960; Farmer and Russell 1964; Russel and Fraser 1994). Indeed, assuming equal absorption coefficients for the different pairs of octahedral cations coordinated to an OH group, a decomposition of the spectra in either the OH-stretching (Besson and Drits 1997a,b; Besson et al. 1987; Drits et al. 1997; Madejova et al. 1992, 1994; Slonimskaya et al. 1986) or OH-bending region (Vantelon et al. 2001) can provide a reasonable estimation of the various populations of octahedral sites in phyllosilicates. We recently applied such an approach to a series of ten montmorillonite samples from different ore bodies (Vantelon et al. 2001) and concluded that most montmorillonite samples presented a nearly random distribution of octahedral cations except for two samples from Wyoming. However, uncertainty in the decomposition of the IR spectra and the absence of observable Fe-Fe-OH vibrations revealed a definite need for complementary spectroscopic studies in

order to refine the mapping of the octahedral sheet of this series of montmorillonite samples.

As shown in various studies on trioctahedral micas (Manceau 1990; Manceau et al. 1988, 1990), dioctahedral micas (Drits et al. 1997), dioctahedral ferruginous smectites (Bonnin et al. 1985; Manceau et al. 1998, 2000a,b) or montmorillonite (Muller et al. 1997), iron edge XAS spectra can provide valuable structural information on both short-range and medium-range order in phyllosilicates, as iron can be easily discriminated from other atoms of the clay layer (Al, Mg and Si). In the present paper we present an Fe K-edge X-ray absorption spectroscopy (XAS) study on a series of montmorillonite samples previously studied by IR spectroscopy and use the combination of these two spectroscopic tools to define the ordering of cations in the octahedral layer of montmorillonite.

Materials

Ten smectites from different origins were selected for this study (Table 1). Montmorillonites from Wyoming (SWy1 and SWy2), Texas (STx1), Arizona (SAz1) and Washington (SWa1) were obtained from the Source Clays Repository of the Clay Mineral Society (University of Missouri). The ferruginous smectite from Washington (SWa1) can be considered as a peculiar montmorillonite with a very high iron content (Komadel et al. 1995). The clay minerals from Bavaria (Bav), China (Chi), Milos (Mil), Georgia (Geo) and North Africa (NAf) were obtained from Iko Erbslöh (Germany). Prior to the study, the montmorillonites were purified by sedimentation and sodium-saturated by three exchanges in molar NaCl solutions. The suspensions were washed with ultrapure water by centrifugation until chloride-free supernatants were obtained. The final solid products were obtained by air-drying. The efficiency of the purification procedure was controlled by X-ray diffraction (XRD) revealing the removal of crystalline kaolinite, quartz and cristobalite. To determine the structural formulae (Table 1), chemical analyses were performed at the Centre de Recherches Pétrographiques et Géochimiques (CRPG) in Vandoeuvre-lès-Nancy, France by ICP measurements using a quantometer Jobin Yvon 70. Mössbauer experiments were performed at Laboratoire de Chimie Physique et Microbiologie pour l'Environnement (LCPME) in Villers-lès-Nancy, France, in order to estimate the oxidation state of iron in the samples. For SWa1, in agreement with previous works (Murad 1987, Komadel et al. 1995), Mössbauer experiments revealed that 2.9% of the total iron was located in poorly crystallized goethite.

Table 1 Origin and structural formulae of the studied montmorillonites

Clay sample	Name	Unit-cell formula per O_{20} OH_4
China	Chi	$(Si_{7.91}Al_{0.09})$ $(Al_{3.11}Mg_{0.79}Fe^{III}_{0.10})$ $Na_{0.88}$
Texas	STx1	$(Si_{7.91}Al_{0.09})$ $(Al_{3.12}Mg_{0.75}Fe^{III}_{0.14})$ $Na_{0.84}$
Arizona	SAz1	$(Si_{7.95}Al_{0.05})$ $(Al_{2.75}Mg_{1.07}Fe^{III}_{0.17})$ $Na_{1.11}$
North Africa	Naf	$(Si_{7.59}Al_{0.41})$ $(Al_{3.28}Mg_{0.44}Fe^{II}_{0.02}Fe^{III}_{0.26})$ $Na_{0.87}$
Georgie	Geo	$(Si_{7.81}Al_{0.19})$ $(Al_{2.85}Mg_{0.79}Fe^{II}_{0.07}Fe^{III}_{0.29})$ $Na_{1.04}$
Wyoming-2	SWy2	$(Si_{7.74}Al_{0.26})$ $(Al_{3.06}Mg_{0.48}Fe^{II}_{0.03}Fe^{III}_{0.42})$ $Na_{0.77}$
Milos	Mil	$(Si_{7.76}Al_{0.24})$ $(Al_{3}Mg_{0.54}Fe^{II}_{0.02}Fe^{III}_{0.44})$ $Na_{0.79}$
Wyoming-1	SWy1	$(Si_{7.73}Al_{0.27})$ $(Al_{3.06}Mg_{0.46}Fe^{II}_{0.03}Fe^{III}_{0.44})$ $Na_{0.76}$
Bavaria	Bav	$(Si_{7.83}Al_{0.17})$ $(Al_{2.78}Mg_{0.65}Fe^{II}_{0.05}Fe^{III}_{0.52})$ $Na_{0.86}$
Washington	SWa1	$(Si_{7.42}Al_{0.58})$ $(Al_{1.03}Mg_{0.27}Fe^{III}_{2.7})$ $Na_{0.85}$

Method: X-ray absorption spectroscopy

Data collection

Fe K-edge measurements were performed on the D44 station of the DCI storage ring (1.85 GeV and 300 mA) at LURE (Orsay, France), using Si(511) and Si(111) double-crystal monochromators for XANES and EXAFS, respectively. The monochromator was calibrated by reference to metallic iron (Fe K-edge at 7112 eV). For each sample, six individual EXAFS spectra were collected in the transmission mode at 77 K over the 7000–8300-eV energy range with 2-eV steps and 2 s collection time. For XANES measurements, two or three spectra were collected over the 7090–7210-eV energy range with 0.2-eV steps and 2 s collection time. A metallic iron foil spectrum was recorded before and after each sample for accurate energy calibration.

Data analysis

EXAFS oscillations were reduced from raw data using standard procedures (Teo 1986) with software written by Michalowicz (1990): the background contribution prior to the absorption edge was fitted with a linear function μ_0 and subtracted from the absorbance spectrum μ. The post edge background absorption was fitted with a polynomial function μ_1 (degree 5) within the energy range 7168–8300 eV. The EXAFS oscillations were finally calculated following the formula $\chi(E) = [\mu(E) - \mu_1(E)]/[\mu_1(E) - \mu_0(E)]$, and using the Lengeler–Eisenberger method: $\mu_1(E) - \mu_0(E) = [\mu_1(E^0) - \mu_0(E^0)] * [1 - 8(E - E^0)/3E^0]$, taking E^0 in the rising edge, $E^0 = 7122$ eV. Radial distribution functions (RDFs) uncorrected for phase shifts were calculated with a Fourier transformation of $k^3\chi(k)$ spectra using a Kaiser window (shape factor $\tau = 3$) in the [3.6–14] $Å^{-1}$ k range. Uncorrected distances are referred to as R^*.

Theoretical simulations

In order to generate theoretical XAS spectra, a crystallographical model of montmorillonite has to be used. Two K-montmorillonite models were proposed by Tsipursky and Drits (1984) on the basis of electron diffraction data: a *trans*-vacant model *MT* and a *cis*-vacant model *MC* corresponding to *C*2/*M* and *C*2 space groups, respectively. As revealed by thermal analyses (Vantelon 2001), and more precisely by the position of the dehydroxylation peak, all the smectites used in the present study, except the sample from Washington, are mainly *cis*-vacant. In the *trans*-vacant model *MT*, the two *cis*-occupied sites are crystallographically identical, and therefore, only one octahedral cationic position is required to build up the octahedral sheet. In contrast, in the *MC* model, the octahedral cations occupy both *trans* and *cis* octahedral positions. The *MT* model could not be used in the case of the sample SWa1, as no distinction could be made between Al and Fe octahedral sites.

The *MC* model was then selected for theoretical simulations of all the clays. Its main features are presented in Fig. 1. Three different positions describe octahedral sites, *M*1, *M*2 and *M*3. *M*1 and *M*2 are occupied *cis* and *trans* sites respectively, whereas *M*3 is a vacant *cis* site. The crystallographic dimensions of the model are $a = 5.2$ Å, $b = 9.2$ Å, $c = 10.13$ Å and $\beta = 99°$. A montmorillonite cluster was then generated from the *MC* model using the ATOMS 7.02 code, the absorbing iron atom being placed in the *M*1 site. The various single and multiple scattering paths in this cluster and their respective backscattering efficiency and magnitude, as well as the corresponding theoretical khi(k) spectra, were then obtained using the FEFF7.02 program (Mustre de Leon et al. 1991). As the differences in backscattering amplitudes between Si, Al and Mg are very limited, these three atoms were considered as identical backscatterers and the montmorillonite model was simplified accordingly, using aluminium and iron only in the octahedral layer and silicon only in the tetrahedral layer. The obtained distances and neighbour numbers are coherent with those reported in the literature for dioctahedral clay structures (Manceau et al. 1998, 2000a, b). The different scattering paths, generated by FEFF, are used by the FEFFIT code to fit experimental data (Newville et al. 1995). The contribution of each scattering path, without distinction between single- or multiple-scattering paths, can be adjusted by applying standard EXAFS parameters such as neighbour number (N_i) and distance (R_i), Debye–Waller factor (σ_i), and shift in energy origin (ΔE), until the best fit to the experimental data is found. Fit quality was indicated by the *r* factor and χ^2_vvalues (see Appendix); and $r \leq 0.02$ and $\chi^2_v > 10$, are common conditions for good fits to carefully measured data on concentrated samples. For the fitting procedure, the R_i and σ_i values were freed. The energy shift value was fixed to the value obtained after the fitting of the first shell of neighbours (six oxygen atoms). The coordination numbers (Fe–Fe and Fe–Al pairs) were fixed by the operator, following several criteria: the distances between two octahedral cations should not be out of the range 2.9–3.2 Å; the Debye-Waller term σ_i values should not be very different for Fe–Al and Fe–Fe, as they express crystallographic disorder; the different features on the k^3*khi(k) curve should be fitted to the best.

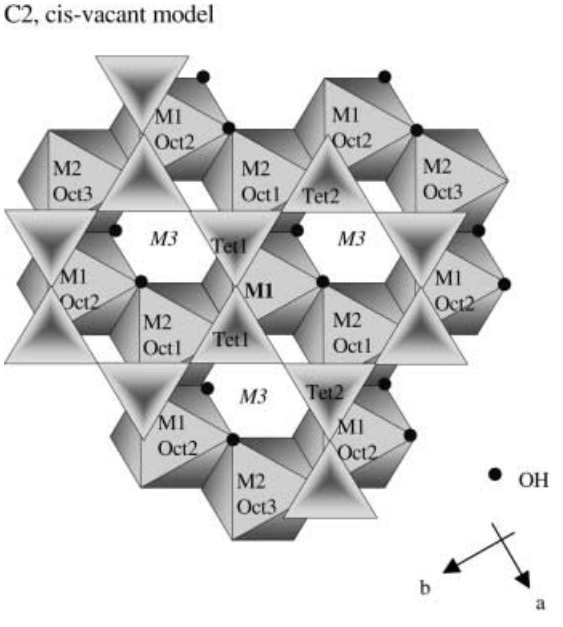

Fig. 1 Clay layer model for theoretical simulations. *M1 in bold characters* is the central iron atom, located in *cis*-octahedral position. *Oct1*, *Oct2* and *Oct3* correspond to the three shells of octahedral cations at 3.1, 5.2–5.3 and 6–6.2 Å, respectively. *Tet 1* and *Tet 2* represent half of the two first tetrahedral cation neighbours at 3.17–3.25 and 4.3 Å, respectively

Results

XANES results

In agreement with literature results obtained on related clay minerals (Bonnin et al. 1985; Paris et al. 1991; Brigatti et al. 2000; Manceau et al. 2000b), the edge crest position on the XANES Fe K-edge spectra reveals that Fe(III) is the main oxidation state of iron in the present montmorillonites, which confirms the proposed unit-cell formulae (Table 1).

Furthermore, pre-edge peaks are very small, as usually encountered for iron in octahedral sites (Manceau et al. 2000b; Petit et al. 2001). Their splitting into $3d$-t_{2g} and $3d$-e_g-like components with a separation of about 1.5 eV further confirms octahedral coordination.

EXAFS results

The experimental EXAFS signals obtained for the different clays are plotted in Fig. 2, and are ordered from top to bottom according to increasing iron content. Montmorillonites with low iron contents (Chi, STx1 and SAz1) exhibit a low signal/noise ratio for high k values. Marked differences can be observed between the signal corresponding to SWa1 and other curves, particularly at 4.5, 6.5, 8 and 10 $Å^{-1}$.

RDF curves, uncorrected for phase shifts (Fig. 3), present one first peak centred at 1.6 Å, assigned to oxygen atoms surrounding octahedral iron. For higher distances, all samples except SWa1 exhibit two less intense peaks. For the Washington sample, a single second peak centred at 2.8 Å is observed, with an intensity

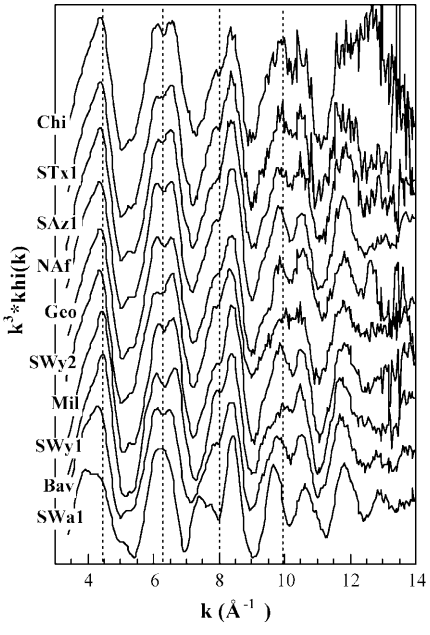

Fig. 2 Experimental Fe K-edge EXAFS oscillations

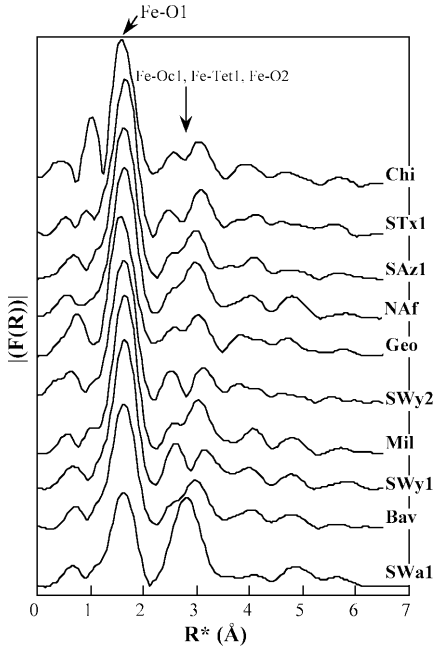

Fig. 3 Radial distribution functions [calculated for (3.7–14) $Å^{-1}$ k range with a Kaiser window $\tau = 3$]

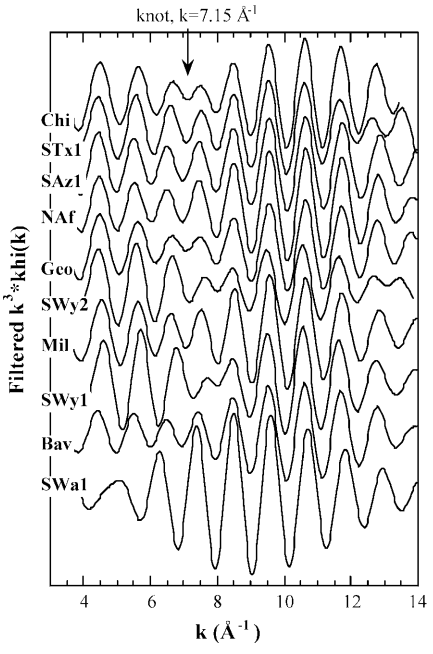

Fig. 4 Filtered k3*khi(k) curves calculated by inversed Fourier transform in the (1–3.4) Å R^* range

roughly equal to that of the first peak. The features observed in the [2–3.4] Å R^* range, can be assigned to the sum of three different shells of neighbours (Fig. 1) (1) three octahedral cations Oct1, (2) four tetrahedral cations Tet1 and (3) two oxygen atoms O2 (Manceau et al. 1998, 2000a,b). The particular RDF observed for SWa1 in this region is certainly due to the high iron content of this clay, the backscattering signal from iron being more intense than those due to lighter atoms such as Mg and Al. The other nine samples present either one peak with a shoulder on the low distance side (SAz1, Naf, Mil, Bav) or two well-separated peaks (Chi, STx1, Geo, SWy2, SWy1) with no evident link with iron content. Upon further examination of the curves, it appears that the ten samples can, in fact, be classified into four subgroups according to the shape and position of the second peak: SWa1 with a single high peak centred at 2.80 Å; NAf, Mil and Bav with a peak at 2.97 Å and a weak shoulder at 2.55 Å; Chi, STx1, Geo with a peak at 3.03 Å and a shoulder at 2.55 Å; and SWy1, SWy2 with a doublet at 2.50–2.60 and 3.13 Å.

For further analysis, the deconvoluted signals of the [2–3.4] Å R^* range, obtained by back-Fourier calculation, are shown in Fig. 4. Except for SWa1, a knot can be observed on the filtered k^{3*}khi(k) curves. This knot is due to interferences between backscattering waves issued from two shells of the same atom located at two different distances $R1$ and $R2$ from the absorbing iron atom. The k_{knot} position follows the relation (Teo 1986) $k_{knot} = \pi/2\Delta R$ where $\Delta R = |R2-R1|$. This knot, located at about 6.5–7 $Å^{-1}$ for Chi, STx1, SAz1, NAf, Geo, Mil and Bav, shifts towards high k values (about 8 $Å^{-1}$) for the Wyoming samples SWy1 and SWy2. Therefore, the difference in bonding distances is around 0.25 Å for most samples and 0.2 Å for the Wyoming clays. The distribution of shells from the montmorillonite model indicates that the first-nearest cationic shell corresponds to octahedral cations located at about 3.00 Å, whereas the second-nearest shell, which corresponds to silicon in tetrahedral sites, is located around 3.20 Å. For low-iron montmorillonites, the octahedral cations are mainly aluminium and magnesium. As silicon, aluminium and magnesium atoms give a very close backscattering signal, the observed knot corresponds to an interference between backscattering waves from octahedral and tetrahedral cations. Substitution of octahedral cations by iron modifies the interference fingerprint, shifts the knot towards high k values and even suppresses it when iron is the major octahedral cation, as for SWa1. Such a phenomenon was also observed by Manceau (1990) on a phlogopite–annite series.

Theoretical simulations

Nature of nearest octahedral cations

In a first step, we compared the theoretical curves obtained with (1) three aluminium atoms, (2) one iron and two aluminium atoms and (3) one aluminium and two iron atoms as nearest octahedral neighbours (Fig. 5), all other variables being constant. For three Al atoms, the second peak of the RDF is a small intense doublet at 2.5 and 3.1 Å (Fig. 5b). For one Fe and 2 Al, the peak shape evolves towards a main peak at 3.0 Å with a shoulder at 2.5 Å. Finally, for two Fe and 1 Al, the second peak becomes a single intense peak around 2.9 Å. These three simulations are in agreement with the

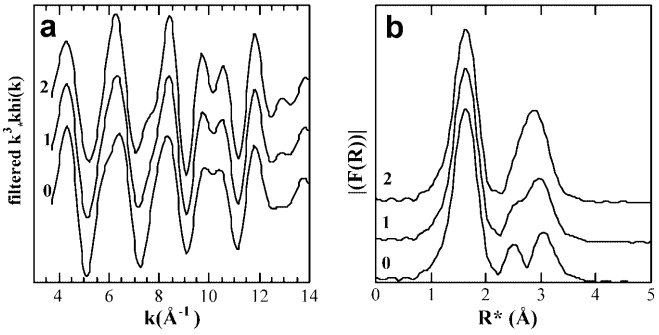

Fig. 5a, b Theoretical calculations of EXAFS spectra. Variation of first nearest octahedral cations nature, **a** EXAFS oscillations. **b**. RDFs. *0* 3 Al cations, no Fe; *1* 2 Al and 1 Fe cations; *2* 1 Al and 2 Fe cations

observed increase of the second peak of the RDF in SWa1. Concerning the EXAFS signal (Fig. 5a), iron substitution results in several modifications. It decreases the first oscillation maximum at 4.5 $Å^{-1}$, sharpens the second oscillation at 6 $Å^{-1}$, generates a shoulder at 7.5 $Å^{-1}$, emphasizes the fourth oscillation splitting at 10 $Å^{-1}$ and generates a new structure at 13 $Å^{-1}$. Such features are indeed observed on the experimental spectra (Fig. 2)

Nature of octahedral cations in higher distance shells

In order to check if valid information about the nature of second-nearest octahedral cations Oct2 (Fig. 1) could be obtained, the fitting procedure was also carried out in the [1–5.4] Å R^* range. Several tests were then run to check the influence of the number of iron backscattering atoms in the Oct2 shell (six octahedral cations at 5.2–5.28 Å). Three different situations were simulated as (1) five Al and one Fe, (2) four Al and two Fe and (3) two Al and four Fe. It appears that increasing iron occupancy at high distances has only a limited effect on the obtained RDFs. In addition, in this range, multiple-scattering events strongly affect the signals for $R^* = 4$ Å,

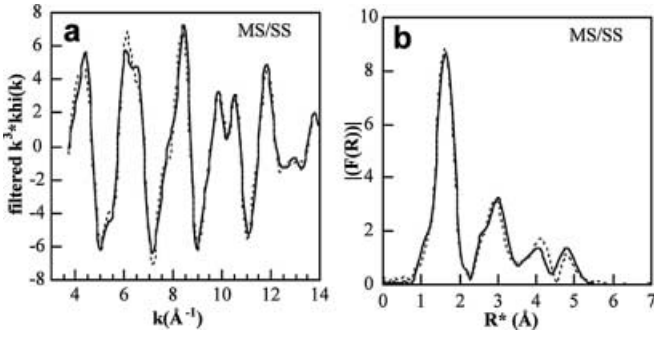

Fig. 6 Comparison of theoretical curves calculated with multiple scattering (*solid line*) or with only simple scattering (*dotted line*). **a** Filtered k^3*khi(k) in the [1–5.4] Å R^* range. **b** RDF

as shown in Fig. 6, which compares theoretical curves calculated with and without multiple scattering.

In view of these results and taking into account the heterogeneity of natural clay samples, it would then seem rather irrelevant to perform fitting in a large R range. We then decided to limit our fitting procedure to the range [1–4] Å, taking into account the 13 paths displayed in Table 2. In this range, the nature of interlayer cations (Na in the samples, K in the model) and their hydration state do not affect the fitting results, as the interlayer region is not included in the considered distance range. The first shell around octahedral cations is simplified as one single shell of six oxygen atoms at 2.00–2.02 Å. The same type of simplification is applied to the nearest tetrahedral neighbours, where one single shell of four silicon atoms at 3.21–3.26 Å is taken into account.

Fitting results

The comparisons between experimental and theoretical curves [filtered k^3*khi(k) and Fourier transform] are shown in Fig. 7 and the corresponding values of the single-scattering paths are reported in Table 3. In all cases the experimental k^3*khi(k) and RDFs are well reproduced by the simulated spectra, in the chosen range $1 \leq R^* \leq 3.4$ Å. As XANES spectra showed that all iron atoms were located in octahedra, the number of oxygen atoms in the first coordination shell was fixed at six, while the bonding distance, R(Fe–O1), and Debye–Waller term, σFe–O1, were released for fitting. In all samples, the Fe–O bonding distances are in the range between 2.00 and 2.02 Å, typical values for octahedral ferric cations. The values of the Debye–Waller factor are 0.06, except for the samples Geo, Bav and SWa1, which display slightly higher σFe–O1 values, suggesting some lowering of site symmetry.

The parameters of the higher-distance shells were adjusted by fixing the number of neighbours N for each path, and releasing distance and σ values. In the case of

Table 2 Paths list as generated by FEFF7.02. N is the degeneresence number of the path, *nleg* is the number of legs (*2* for single scattering, *3* for double scattering)

Path index	Scattering atom(s)	N	*nlegs*	*r* effective (Å)
1	O1	6	2	1.96
2	Oct1/M2 : Al	1	2	2.95
3	Oct1/M2 : Fe	2	2	3.08
4	Tet1 : Si	4	2	3.17
5	O2	2	2	3.26
6	O–O	4	3	3.26
7	O–O	4	3	3.38
8	Si–O	4	3	3.38
9	Al–O	4	3	3.41
10	Si–O	4	3	3.42
11	O3	2	2	3.69
12	O3	2	2	3.76
13	O3	2	2	3.83

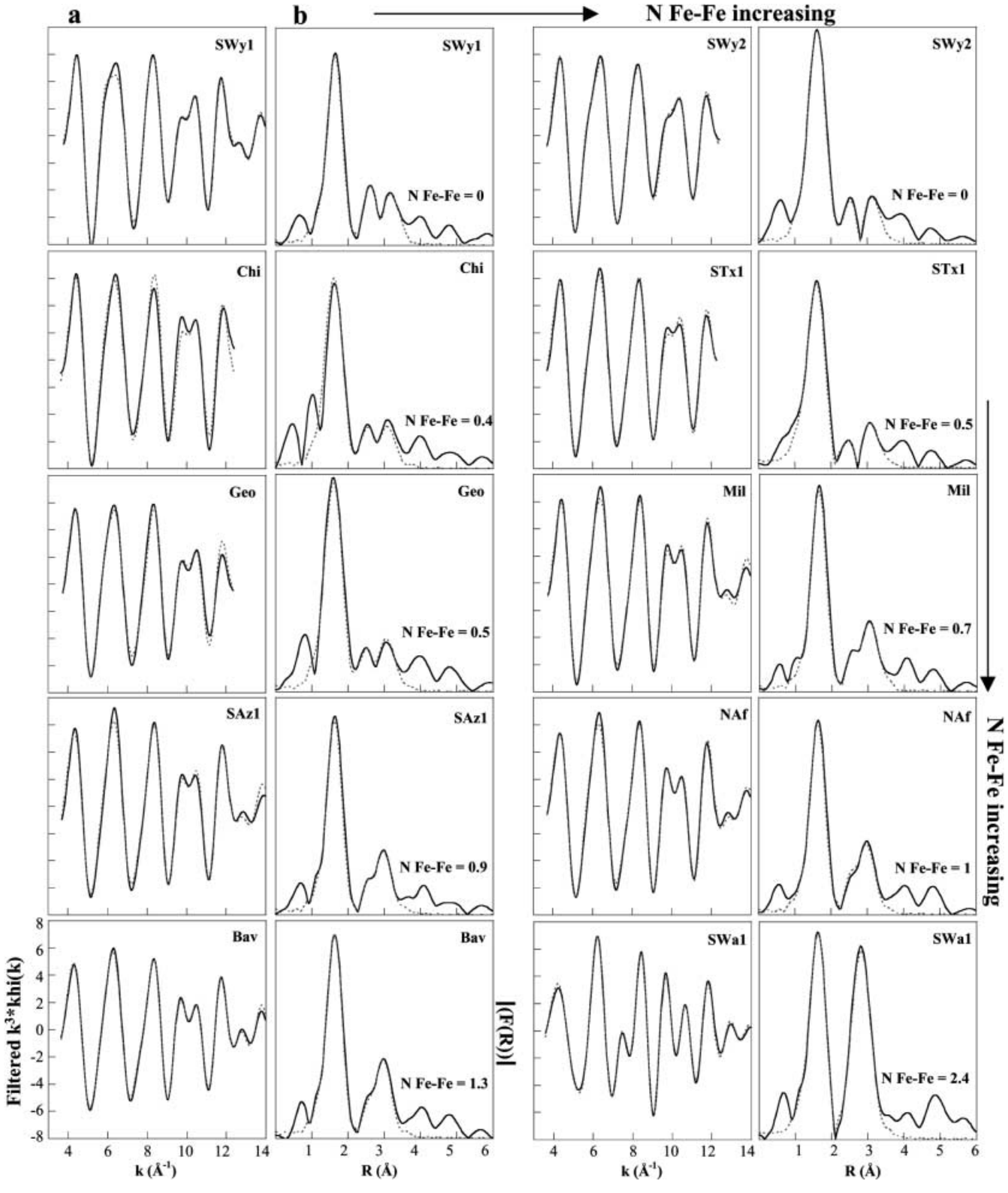

Fig. 7 Comparison of experimental (*solid line*) and theoretical (*dotted line*) curves a: filtered k^3*khi(k). **b** RDF, modulus. Plots are positioned following increase of iron–iron pairs, *from left to right* and *from top to bottom*

the first octahedral cation shell, the final numbers of Al–Fe and Fe–Fe pairs (always adding 3) were manually adjusted in order to obtain close σ values for these two

Table 3 Fitting results, $S_0^2 = 0.87, \Delta E = 0.33$ eV, $\chi_v^2 > 10$, * see Appendix

Clay	Chi	STx1	SAz1	NAf	Geo	SWy2	Mil	SWy1	Bav	SWa1
N O1	6	6	6	6	6	6	6	6	6	6
R Fe–O1	2.00	2.00	2.00	2.01	2.00	2.00	2.01	2.01	2.01	2.02
σ Fe–O1	0.06	0.06	0.06	0.06	0.07	0.06	0.06	0.06	0.07	0.08
N Al	2.6	2.5	2.1	2	2.5	3	2.3	3	1.7	0.8
R Fe–Al	3.02	3.04	3.03	3.01	3.01	3.03	3.02	3.03	3.06	3.02
σ Fe–Al	0.06	0.07	0.06	0.06	0.07	0.07	0.06	0.06	0.06	0.08
N Fe	0.4	0.5	0.9	1	0.5	0	0.7	0	1.3	2.2
R Fe–Fe	3.11	3.11	3.12	3.1	3.12	–	3.14	–	3.11	3.09
σ Fe–Fe	0.06	0.06	0.06	0.06	0.07	–	0.06	–	0.07	0.07
N Si	4	4	4	4	4	4	4	4	4	4
R Fe–Si	3.25	3.23	3.21	3.2	3.21	3.22	3.2	3.26	3.25	3.24
σ Fe–Si	0.08	0.09	0.07	0.09	0.10	0.09	0.08	0.09	0.09	0.08
N O2	2	2	2	2	2	2	2	2	2	2
R Fe–O2	3.28	3.33	3.33	3.36	3.36	3.37	3.38	3.24	3.33	3.34
σ Fe–O2	0.07	0.07	0.10	0.09	0.10	0.10	0.06	0.08	0.07	0.10
*r factor	0.04	0.013	0.017	0.012	0.023	0.009	0.017	0.009	0.007	0.008

distances. The calculated distances are very similar from one sample to another. The Fe–Al distances vary between 3.01 and 3.06 Å, whereas the Fe–Fe ones lie in the range 3.09–3.14 Å. All these values are consistent with previous literature results (Bonnin et al. 1985; Decarreau et al. 1987; Manceau et al. 1990, 1998, 2000a). The σ values are close to 0.06 for all samples, except for samples Bav, Geo and SWa1, which exhibit slightly higher σ values, as already observed for the first shell. For the following shells, Fe–Si and Fe–O2, distance and σ values are quite homogenous for all samples and close to the values reported for similar smectite samples (Bonnin et al. 1985; Decarreau et al. 1987; Manceau et al. 1990, 1998, 2000a).

Discussion

EXAFS and RDF curves (Figs. 2, 3) revealed no evident evolution linked to iron content in the montmorillonite layer, but the detailed analysis and simulation of the EXAFS signals (Fig. 7; Table 3) shows that the montmorillonites can be classified according to the number of Fe–Fe pairs in the octahedral layer (Fe ordering). In order to better analyze the observed tendency in terms of crystal chemistry, it is useful to compare the numbers of iron–iron pairs deduced from EXAFS experiments with those deduced from chemical analysis, assuming a random distribution of iron cations within the octahedral sheet (dashed line in Fig. 8). Three distinct situations can then be observed: (1) samples SWy1 and SWy2 do not present any iron–iron pairs, thus revealing an ordered distribution of iron atoms obeying an exclusion rule; (2) samples Chi, Geo, Mil and SWa1 exhibit a slight tendency to iron clustering; (3) samples Bav, NAf, SAz1, and to a lesser extent STx1, exhibit a strong tendency to iron clustering, the number of observed iron–iron pairs being significantly larger than that corresponding to a random distribution. For sample SWa1, the number of iron–iron pairs determined in our EXAFS analysis is slightly higher (2.2) than that obtained (2.0) in a recent paper by Manceau et al. (2000b) who, on the basis of polarized EXAFS experiments, proposed a random distribution of iron atoms in the octahedral layer of the Washington clay.

In order to obtain a more detailed picture of cation distribution in the octahedral sheet, it is useful to combine the results derived from K-edge EXAFS measurements with those obtained from decomposing the IR spectra in the OH- bending region (Vantelon et al. 2001). Table 4 presents a comparison between the expected percentages of Al–Al, Al–Fe and Al–Mg pairs, assuming a random distribution and the amount of cation pairs deduced from the IR analysis. Sample SWa1 was not included in this table because Vantelon et al. (2001) showed that IR analyses in the OH-bending region underestimate the amount of Fe–Fe pairs. In addition, SWa1 is a *trans*-vacant montmorillonite, which prevents a direct comparison with the other samples, which are *cis*-vacant, due to the different relative positions of cations, hydroxyls and vacancies. Nevertheless, a

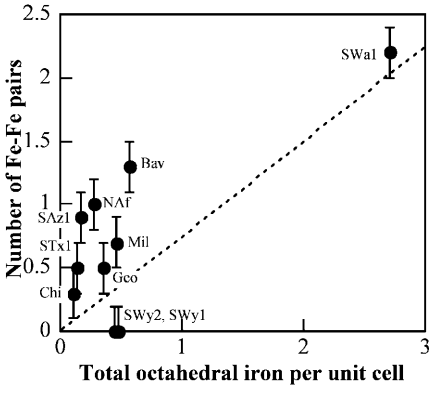

Fig. 8 Number of first iron neighbours calculated from fits as a function of total iron amount (the *dashed line* represents a theoretical random distribution). If the points are located *below the line*, it indicates a tendency towards ordering. On the contrary, points located *above this line* reveal reduced clustering for cation pairs of the same atoms

Table 4 Infrared data. Percentages of cations pairs $P(C_i–C_j)$ calculated for a fully random distribution (*random*) and extracted from OH bending vibration bands deconvolutions (*IR*) (Vantelon et al. 2001).

$i \neq j$

$P(C_i - C_j) = 100 \times \frac{nC_i}{n\text{tot}} \times \frac{nC_j}{n\text{tot}} \times 2$

$i = j$

$P(C_i - C_i) = 100 \times \frac{nC_i}{n\text{tot}} \times \left(\frac{nC_i}{n\text{tot}} - 0.01\right)$

$P(C_i - C_j)$: percentage of cations pairs $C_i - C_j$,
nC_i : number of cations i in the octahedral sheet,
$n$tot : total number of cations in the octahedral sheet.

If the experimental IR value is lower than the random value, it indicates a tendency towards clustering for two different cations, or towards ordering for pairs of the same cation (Al–Al). On the contrary, if the IR value is higher than the random value, it reveals ordering for pairs of different cations, and reduced clustering for cation pairs of the same atoms

	Al–Al–OH		Al–Fe–OH		Al–Mg–OH	
	Random	IR	Random	IR	Random	IR
SWy1	*58*	42	*18*	37	*18*	21
SWy2	*58*	37	*17*	30	*18*	33
Chi	*60*	64	*4*	6	*31*	30
Geo	*50*	61	*13*	10	*28*	29
Mil	*56*	57	*17*	21	*20*	22
STx1	*60*	51	*5*	13	*29*	36
SAz1	*47*	42	*6*	10	*37*	48
Naf	*66*	72	*11*	16	*18*	12
Bav	*48*	45	*20*	21	*23*	34

tendency to clustering of Al and Mg was suggested which would agree with the slight clustering of iron atoms deduced from our EXAFS analyses. For all the other samples, IR measurements (Table 4) confirm the presence of the three subgroups of montmorillonites previously extracted from EXAFS data: (1) the two samples from Wyoming SWy1 and SWy2 exhibit an ordered distribution of Al and Mg cations; (2) samples Geo, Chi and Mil, which present a nearly random distribution of iron atoms, also exhibit a nearly random distribution of light atoms; (3) finally, samples that revealed a clustered iron distribution (STx1, SAz1, NAf and Bav) also exhibit some clustering of light atoms. However, two cases can be distinguished in this latter subgroup. Montmorillonites with a rather low iron content (STx1, SAz1, Naf) exhibit less Al–Al pairs and a higher amount of Al–Fe pairs whereas the Bav sample with a higher iron content exhibits an increase in the number of Al–Mg pairs.

Information resulting from the combination of IR and EXAFS data is summarized in Fig. 9 which presents model schemes of the octahedral layer for SWy1, Mil, SWa1, SAz1 and Bav samples. These schemes were built according to both the number of iron neighbours given by EXAFS analyses and the number of cation pairs given by IR analyses, along the and $[3\bar{1}0]$ and $[\bar{3}\bar{1}0]$ axes for SWy1, Mil, SAz1 and Bav, and along the *b* axis for SWa1. The comparison between Milos and Wyoming samples represents a striking illustration of the diversity of octahedral crystal chemistry, as these two montmorillonites with very similar unit-cell compositions exhibit contrasting cation distributions.

Some additional discussion can be held in the case of the Bavarian sample. Indeed, this sample presents both chemical composition and iron clustering similar to those of the montmorillonite from Camp-Berteaux (Muller et al. 1997). By analogy with this previous work, we could have located Mg atoms in the vicinity of clustered iron atoms. However, in the case of Camp-Berteaux montmorillonite (Muller et al. 1997), the respective location of Mg and Fe atoms was deduced from experiments using Ni as a probe of the octahedral layer. As such experiments were not carried out in our case, we chose rather to present Mg cation distribution that follows the ordering tendency of Mg–Al pairs deduced from IR data.

The pictorial representations in Fig. 9 are only possible model images constrained by EXAFS and IR data. A more precise picture may be obtained by adding some more constraints derived from polarized EXAFS experiments and/or by studying the EXAFS spectra of Ni- or Cu-exchanged montmorillonites after heating at various temperatures (Muller et al., 1997). Furthermore, in all these representations the existence of local trioctahedral domains was never considered in the absence of direct experimental evidence. However, recent EXAFS and ^{19}F MAS-NMR data obtained on synthetic fluorinated montmorillonites (Reinholdt et al. 2001) reveal a local trioctahedral character linked to a clustering of divalent cations. The issue of the existence of magnesian domains in the octahedral sheet of natural montmorillonites then remains an open question. Insights on this problem may be obtained by using ^{19}F MAS-NMR for natural samples in which enough fluorine atoms substitute for OH groups.

In any case, it must be kept in mind that all spectroscopic methods provide only a composition-averaged picture of montmorillonite layers which does not take into account the heterogeneous character of most natural samples. Therefore, a thorough understanding of the crystal chemistry of dioctahedral samples may only be achieved by using well-characterized synthetic clay

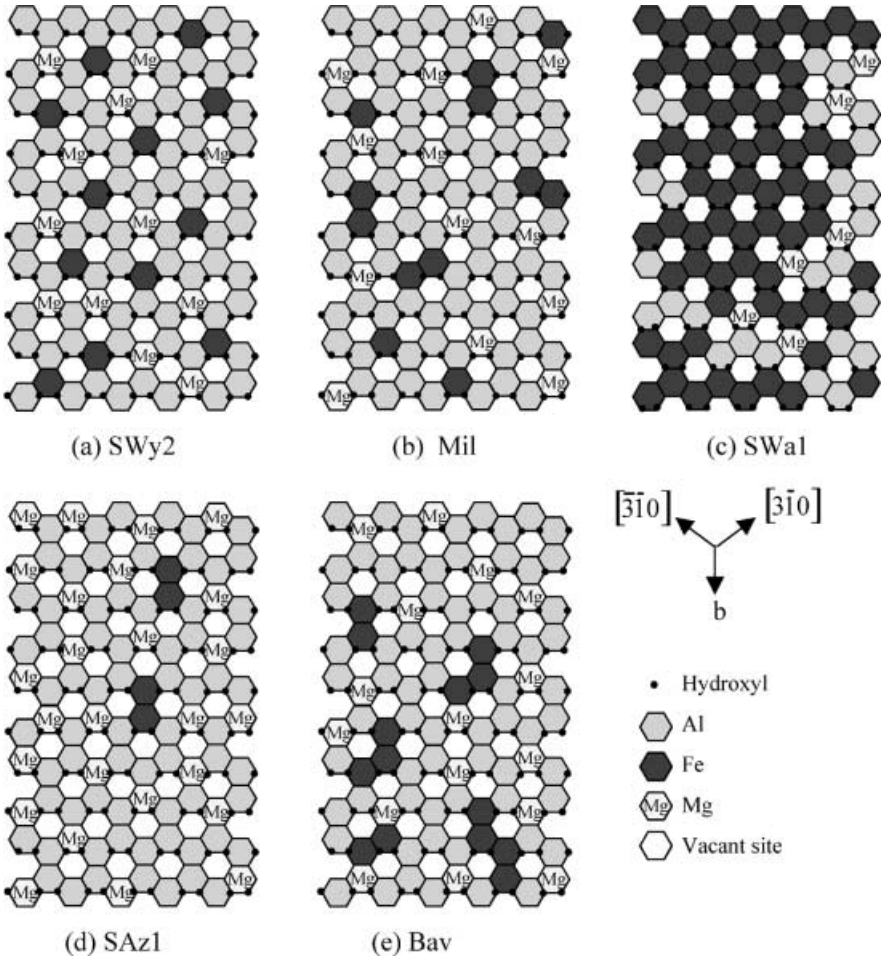

Fig. 9a–e Schematic models of octahedral cations distribution; 100 octahedral cations and 90 cationic pairs. *a* SWy2. *b* Mil. *c* SWa1. *d* SAz1. *e* Bav

samples and by developing new separation protocols allowing various layer types to be discriminated in a given natural clay sample.

Conclusions

Iron EXAFS spectroscopy can be used to study the distribution of iron atoms in montmorillonite samples even for samples with very low iron content. Indeed, the second peak observed in the RDF functions is very sensitive to the relative amount of iron and light atoms surrounding octahedral iron atoms. On the basis of such an analysis, various groups of montmorillonites can be defined according to the degree of iron clustering in the octahedral sheet. In the classification thus obtained, the samples from Wyoming bear a special status as they exhibit a strong ordering of iron cations. In view of such specific ordering, which was also revealed for the other octahedral cations by IR experiments, the choice of Wyoming montmorillonites as reference samples in many clay-related studies appears rather debatable, as they can certainly not be considered as suitable representatives of the montmorillonite group.

The use of IR and EXAFS spectroscopy clearly represents a powerful combination to study the crystal chemistry of dioctahedral montmorillonites. The local-scale information thus obtained should now be analyzed with reference to the geological features of montmorillonite deposits in order to refine the typology of dioctahedral clays.

Appendix

r factor indicates fit quality. It is defined by M. Newville in the FEFFIT Manual, Chapter 5 Goodness of fit and uncertainties in variables, pp 16–20, as

$$\chi^2 = \frac{N_{\mathrm{idp}}}{N\varepsilon^2}\sum_{i=1}^{N}\left[\{\mathrm{Re}[f(R_i)]\}^2+\{\mathrm{Im}[f(R_i)]\}^2\right]$$

$$\chi^2_\nu = \chi^2/\nu$$

$$\nu = N_{\mathrm{idp}} - N_{\mathrm{varys}}$$

$$r = \frac{\sum_{i=1}^{N}\left[\{\mathrm{Re}[f(R_i)]\}^2 + \{\mathrm{Im}[f(R_i)]\}^2\right]}{\sum_{i=1}^{N}\left[\{\mathrm{Re}[\tilde{\chi}_{\mathrm{data}}(R_i)]\}^2 + \{\mathrm{Im}[\tilde{\chi}_{\mathrm{data}}(R_i)]\}^2\right]}$$

$$f(R_i) = \bar{\chi}_{\mathrm{data}}(R_i) - \tilde{\chi}_{\mathrm{model}}(R_i)$$

Re : real part.
Im : imaginary part.

N_{idp} : number of independent variables.
N_{varys} : number of variables in the fit.
N number of function evaluations.
$f(R_i)$ the function to minimize in R space.
ε uncertainty in the measurement.
$\tilde{\chi}_{data}, \tilde{\chi}_{model}$ data and full model EXAFS curves in R space.

References

Besson G, Drits VA (1997a) Refined relationships between chemical composition of dioctahedral fine-grained mica minerals and their infrared spectra within the OH-stretching region, part I. Identification of the OH-stretching bands. Clays Clay Miner 45(2): 158–169

Besson G, Drits VA (1997b) Refined relationships between chemical composition of dioctahedral fine-grained micaceous minerals and their infrared spectra within the OH-stretching region, part II. The main factors affecting OH vibrations and quantitative analysis. Clays Clay Miner 45(2): 170–183

Besson G, Drits VA, Dainyak LG, Smoliar BB (1987) Analysis of cation distribution in dioctahedral micaceous minerals on the basis of IR spectroscopy data. Clay Miner 22: 465–478

Bonnin D, Calas G, Suquet H, Pezerat H (1985) Sites occupancy of Fe^{3+} in Garfield nontronite : a spectroscopic study. Phys Chem Miner 12: 55–64

Brigatti MF, Lugli C, Cibin G, Marcelli A, Gilui G, Paris E, Mottana A, Wu Z (2000) Reduction and sorption of chromium by Fe(II)-bearing phyllosilicates : chemical treatments and X-ray absorption spectroscopy (XAS) studies. Clays Clay Miner 48(2): 272–281

Decarreau A, Colin F, Herbillon A, Manceau A, Nahon D, Paquet H, Trauth-Badaud D, Trescases JJ (1987) Domain segregation in Ni–Fe–Mg smectites. Clays Clay Miner 35: 1–10

Drits VA, Dainyak LG, Muller F, Besson G, Manceau A (1997) Isomorphous cation distribution in celadonites, glauconites and Fe-illites determined by infrared, Mössbauer and EXAFS spectroscopies. Clay Miner 32(2): 153–179

Farmer VC, Russell JD (1964) The infrared spectra of layer silicates. Spectrochim Acta 20: 1149–1173

Fripiat JJ (1960) Applications de la spectroscopie infrarouge à l'étude des minéraux argileux. Bull Gr Franç Arg XII: 25–41

Komadel P, Madejova J, Stucki JW (1995) Reduction and reoxidation of nontronite: questions of reversibility. Clays Clay Miner 43(1): 105–110

Madejova J, Putyera K, Cicel B (1992) Proportion of central atoms in octahedra of smectites calculated from infrared spectra. Geologica Carpathica, series clays 2: 117–120

Madejova J, Komadel P, Cicel B (1994) Infrared study of octahedral site populations in smectites. Clay Miner 29: 319–326

Manceau A (1990) Distribution of cations among the octahedra of phyllosilicates: insight from EXAFS. Can Mineral 28: 321–328

Manceau A, Bonnin D, Kaiser P, Frétigny C (1988) Polarized EXAFS of biotite and chlorite. Phys Chem Miner 16: 180–185

Manceau A, Bonnin D, Stone WEE, Sanz J (1990) Distribution of Fe in the octahedral sheet of trioctahedral micas by polarized EXAFS. Phys Chem Miner 17: 363–370

Manceau A, Chateigner D, Gates WP (1998) Polarized EXAFS, distance-valence least-squares modeling (DVLS) and quantitative texture analysis approaches to the structural refinement of Garfield nontronite. Phys Chem Miner 25: 347–365

Manceau A, Lanson B, Drits V, Chateigner D, Gates W, Wu J, Huo D, Stucki J (2000a) Oxidation-reduction mechanism of iron in dioctahedral smectites, I. Crystal chemistry of oxidized reference nontronites. Am Mineral 85: 133–152

Manceau A, Drits V, Lanson B, Chateigner D, Wu J, Huo D, Gates WP, Stucki J (2000b) Oxidation–reduction mechanism of iron in dioctahedral smectites, II. Crystal chemistry of reduced Garfield nontronite. Am Mineral 85: 153–172

Michalowicz A (1990) Methods and softwares for X-ray absorption spectra analysis. Applications for studying local order and crystalline disorder in inorganic materials [Méthodes et programmes d'analyse des spectres d'absorption des rayons X (EXAFS). Applications à l'étude de l'ordre local et du désordre cristallin dans les matériaux inorganiques]. PhD Thesis, Université Paris Val de Marne

Muller F, Besson G, Manceau A, Drits VA (1997) Distribution of isomorphous cations within octahedral sheets in montmorillonite from Camp-Berteau. Phys Chem Miner 24: 159–166

Murad E (1987) Mössbauer spectra of nontronites: structural implications and characterization of associated iron oxides. Zeits Pflanzenernaehr Bodenk 150: 279–285

Mustre de Leon J, Rehr JJ, Zabinsky SI, Albers RC (1991) Ab initio curved-wave X-ray absorption fine structure. Phys Rev (B) 44: 4146

Newville N, Ravel B, Haskel D, Rehr JJ, Stern EA, Yacoby Y (1995) Analysis of multiple-scattering XAFS data using theoretical standards. Physica (B) 208 & 209: 154–155

Paris E, Mottana A, Mattias P (1991) Iron environment in a montmorillonite from Gola del Furlo (Marche, Italy). A synchrotron radiation XANES and a Mössbauer study. Mineral Petrol 45:105–117

Petit PE, Farges F, Wilke M, Solé VA (2001) Determination of the iron oxidation state in Earth materials using XANES pre-edge information. J Synchrotron Rad 8: 952–954

Reinholdt M, Miehe-Brendle J, Delmotte L, Tuilier MH, le Dred R, Cortes R, Flank AM (2001) Fluorine route synthesis of montmorillonites containing Mg or Zn and characterization by XRD, thermal analysis, MAS-NMR and EXAFS spectroscopy. Eur J Inorg Chem 11: 2831–2841

Russell JD, Fraser AR (1994) Infrared methods. In: Wilson MJ (ed) Clay mineralogy: spectroscopic and chemical determinative methods. Chapman & Hall, London, p 11–67

Slonimskaya MV, Besson G, Dainyak LG, Tchoubar C, Drits VA (1986) Interpretation of the IR spectra of celadonites and glauconites in the region of OH-stretching frequencies. Clay Miner 21: 377–388

Teo BK (1986) EXAFS: basic principles and data analysis. Springer, Berlin Heidelberg New York

Tsipursky SI, Drits VA (1984) The distribution of octahedral cations in the 2:1 layers of dioctahedral smectites studied by oblique-texture electron diffraction. Clay Miner 19: 177–193

Vantelon D (2001) Spatial distribution of cations in octahedral sheet of montmorillonites: consequences on colloidal properties [Répartition des cations dans la couche octaédrique des montmorillonites : répercussions sur les propriétés colloidales]. PhD Thesis, INPL Nancy

Vantelon D, Pelletier M, Michot LJ, Barres O, Thomas F (2001) Fe, Mg and Al distribution in the octahedral layer of montmorillonites. An infrared study in the OH-bending region. Clay Miner 36: 369–379